Supporting Information

Strain-Tunable Opto-electronics in PdS_2 Monolayer: the Role of Band Nesting and Carrier-Phonon Scattering

Hongfa Wang[1,2], Yancheng Gong[1,2], Subrahmanyam Pattamatta[3], Junwen Li[4], and Hailong Wang[1,2,‡], Zhizi Guan[3,†]

[1]CAS Key Laboratory of Mechanical Behavior and Design of Materials, Department of Modern Mechanics, University of Science and Technology of China, Hefei, Anhui 230027, China
[2]State Key Laboratory of Nonlinear Mechanics, Institute of Mechanics, Chinese Academy of Science, 15 Beisihuan West Road, Beijing 100190, China
[3]Department of Mechanical Engineering, The University of Hong Kong, Hong Kong, China
[4]DFTWorks LLC, Oakton, VA 22124, USA
† zhiziguan@connect.hku.hk
‡ hailwang@ustc.edu.cn

Mechanical Stability

To check the mechanical stability of PdS_2 monolayer, we carry out the calculations of elastic constants ($C_{11} = 57.42\ N/m$, $C_{12} = 3.09\ N/m$, $C_{22} = 79.46\ N/m$, $C_{66} = 24.0\ N/m$). The elastic constants satisfy Born-Huang stability criteria as described by:

$$C_{11} > 0,\ C_{66} > 0,\ C_{11} * C_{22} > {C_{12}}^2$$

The results confirm that PdS_2 monolayer is mechanically stable.

Scissor Operator Approximation

To evaluate the impact of HSE06 functional on the optical response, we employed the scissor operator approximation [1, 2], which rigidly shifts the conduction bands to match the HSE06 band gap while renormalizing the optical transition matrix elements to satisfy sum rules (i.e., rescaling the matrix elements by $\Delta E_{HSE}/\Delta E_{PBE}$). This PBE+scissor approach is significantly more cost-effective than a full HSE06 calculation while providing comparable accuracy for band-gap-dependent properties [3, 4].

We performed this scissor correction to benchmark our results. As shown in Fig. S6, the scissor-corrected main absorption peak undergoes a blueshift as expected, while the overall spectral features remain unchanged. This result confirms that the band nesting feature governing the optical response is robust and well captured by PBE, despite the band gap underestimation. Given that our study focuses on the strain-induced evolution of the primary absorption features rather than the absolute magnitude of the optical gap and the dielectric response, the PBE functional is sufficient to capture the essential physics.

SERTA Carrier Mobility

To achieve a comprehensive understanding and accurate evaluation of the charge transport properties, we go beyond the deformation potential theory and solve the linearized Boltzmann Transport Equation (BTE) using the Self-Energy Relaxation Time Approximation (SERTA) [5] with full first-principles electron-phonon coupling. In this framework, the carrier mobility $\mu_{\alpha\beta}$ is calculated as:

$$\mu_{\alpha\beta} = \frac{1}{n_c \Omega} \mathcal{L}_{\alpha\beta}^{(0)},$$

where Ω is the unit cell volume, and $n_c$is the carrier concentration defined as $n_c = \sum_n \int_{BZ} \left(\frac{dk}{\Omega_{BZ}}\right) f_{nk}$ with the summation running over the conduction (valence) bands for electrons (holes). The transport coefficient $\mathcal{L}_{\alpha\beta}^{(0)}$ is:

$$\mathcal{L}_{\alpha\beta}^{(0)} = -\sum_n \int \left(\frac{dk}{\Omega_{BZ}}\right) v_{nk,\alpha} v_{nk,\beta} \tau_{nk} \left(\frac{\partial f_{nk}}{\partial \varepsilon}\right),$$

where f_{nk} is the Fermi-Dirac distribution function, and v_{nk} are the velocity matrix elements computed using the commutator of the Hamiltonian with the position operator to include the non-local pseudopotential contribution:

$$v_{nk} = < \psi_{nk} | \hat{p} + i[V^{nl}, r] | \psi_{nk} >.$$

Here, $\hat{p}$ is the momentum operator and v_{nk} is the non-local part of the pseudopotential. Consequently, the carrier relaxation time τ_{nk} is determined by the total scattering rate from all phonon modes:

$$\frac{1}{\tau_{nk}} = \left(\frac{2\pi}{\hbar}\right) \sum_{m,\nu} \int_{BZ} \left(\frac{dq}{\Omega_{BZ}}\right) |g_{mn\nu}(k,q)|^2 \times \left[\left(n_{q\nu} + f_{mk+q}\right)\delta\left(\varepsilon_{nk} - \varepsilon_{mk+q} + \hbar\omega_{q\nu}\right) + \left(n_{q\nu} + 1 - f_{mk+q}\right)\delta\left(\varepsilon_{nk} - \varepsilon_{mk+q} - \hbar\omega_{q\nu}\right)\right],$$

where $g_{mn\nu}(k,q)$ are the electron-phonon matrix elements describing the coupling strength. f_{nk} (and f_{mk+q}) and $n_{q\nu}$ are the Fermi-Dirac and Bose-Einstein distribution functions, respectively.

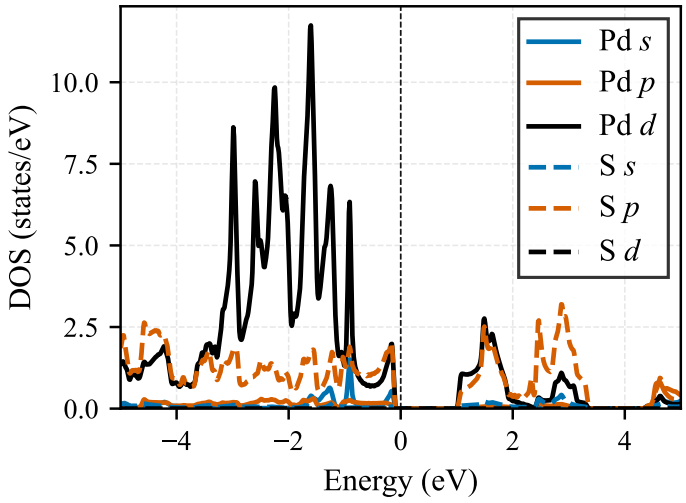

Fig. S1. Projected Density of States (PDOS) of PdS_2 monolayer.

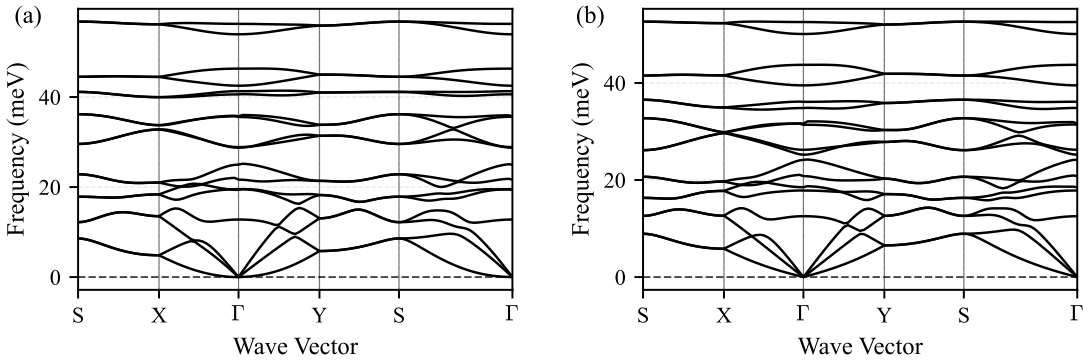

Fig. S2. Phonon dispersion of the PdS_2 monolayer: (a) 0% biaxial strain and (b) 4% biaxial tensile strain.

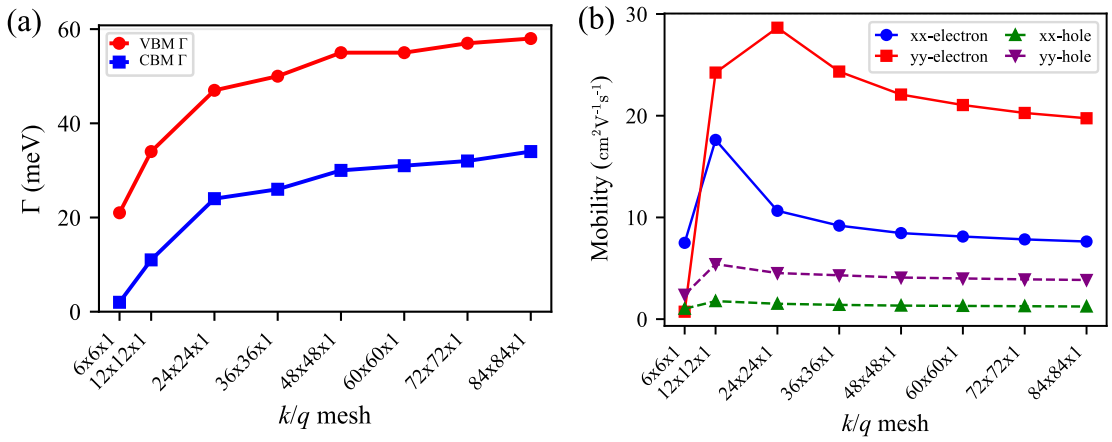

Fig. S3. Convergence tests with respect to *k*/*q* mesh: (a) carrier linewidth at Γ point and (b) carrier mobility.

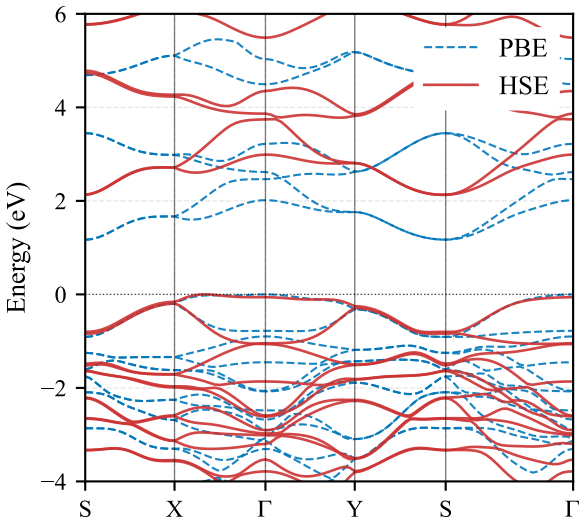

Fig. S4. Comparison of the electronic band structures calculated using PBE and HSE06 functionals.

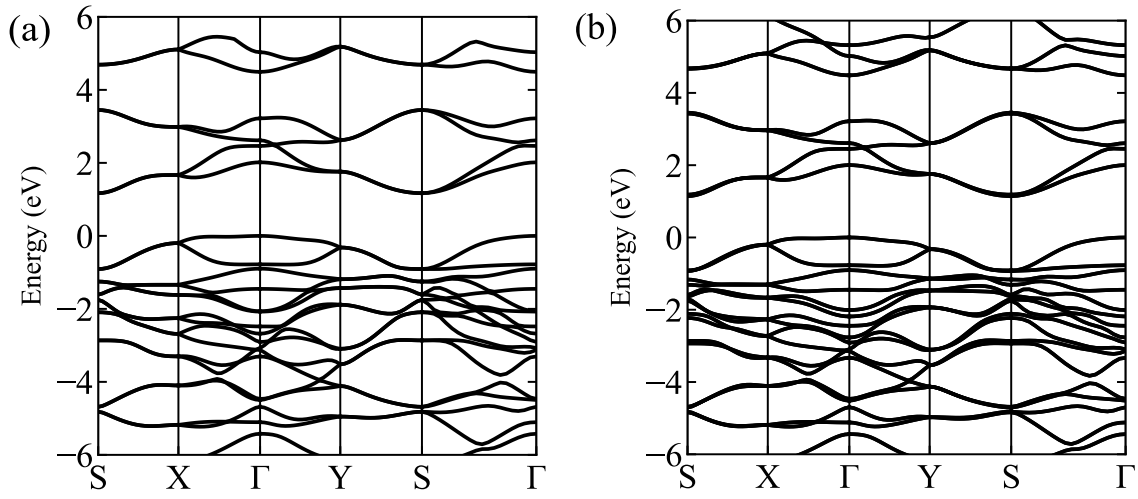

Fig. S5. Electronic band structures of PdS_2 monolayer calculated (a) without and (b) with the inclusion of spin-orbit coupling (SOC) effect. The nearly identical band profiles in both panels indicate that the SOC effect is negligible.

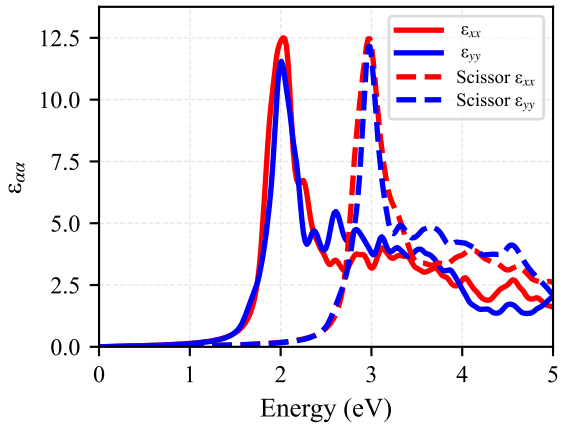

Fig. S6. Comparison of the imaginary part of the dielectric function calculated using PBE and the scissor-corrected method (Scissor).

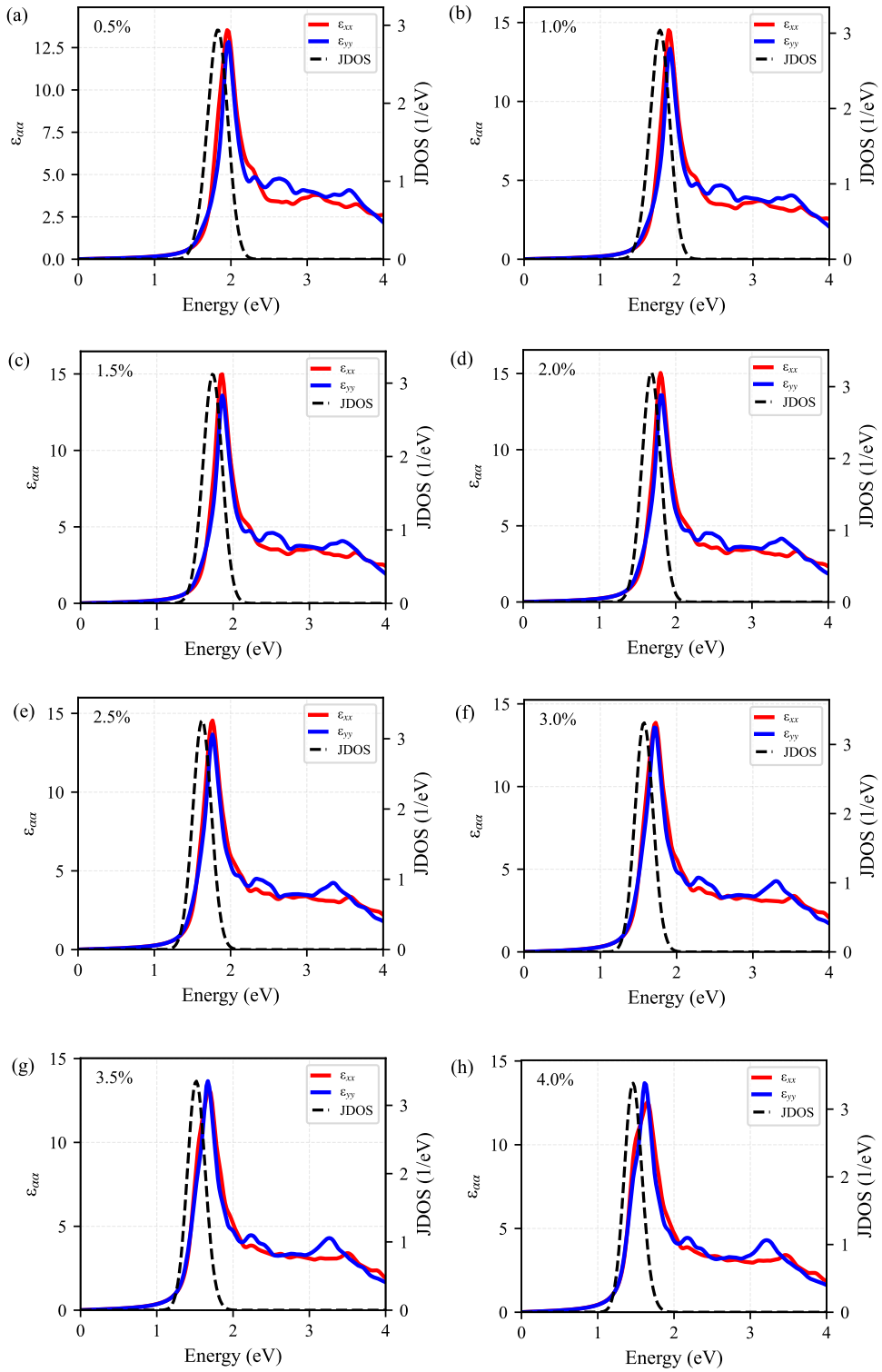

Fig. S7. Imaginary part of the dielectric function (left vertical axis) and joint density of states (JDOS, right vertical axis) between the highest valence band and lowest conduction band of PdS_2 monolayer under different biaxial strain.

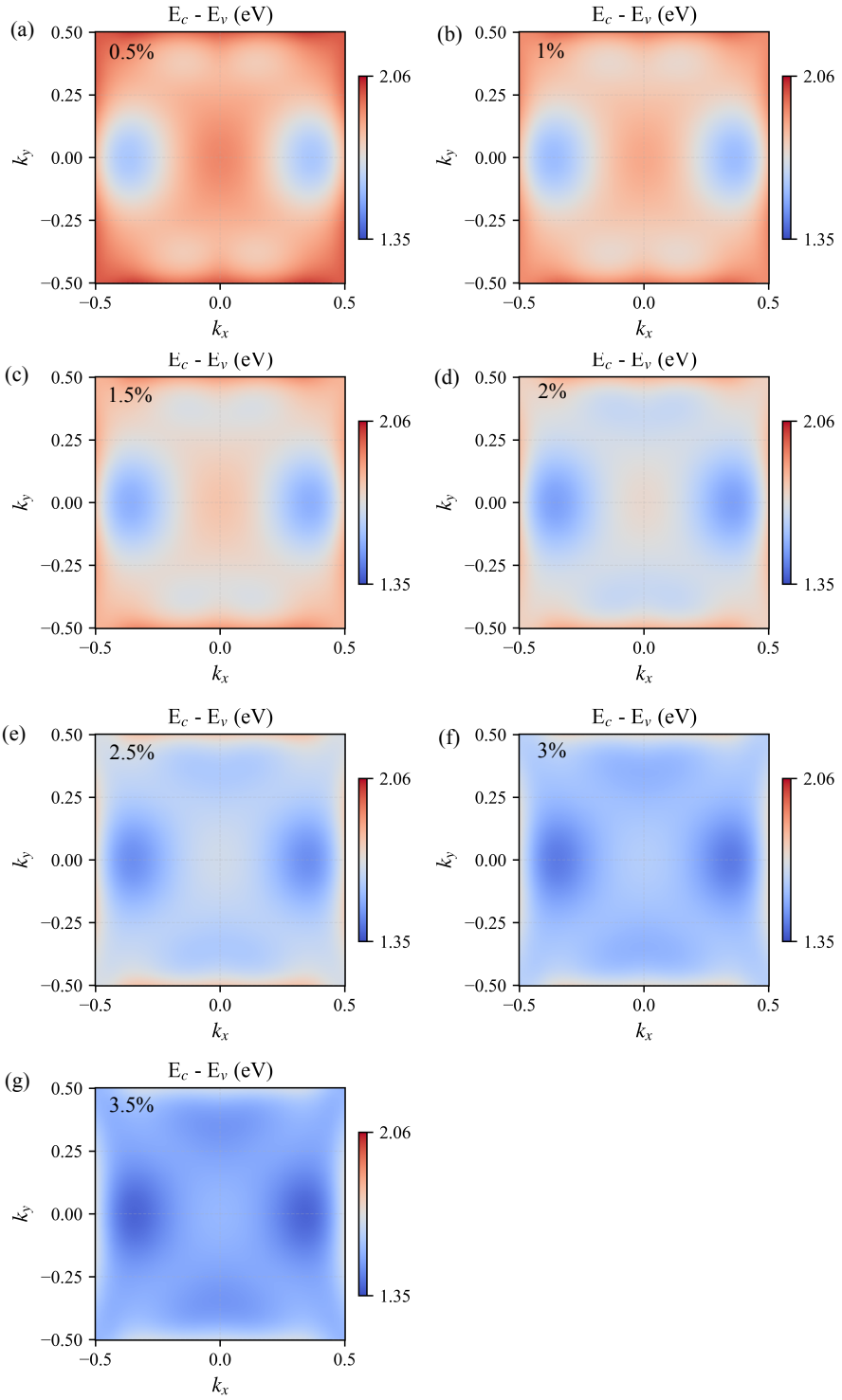

Fig. S8. Band energy difference heat map of PdS_2 monolayer between highest valence band (VB) and conduction band (CB) of PdS_2 monolayer under different biaxial strain.

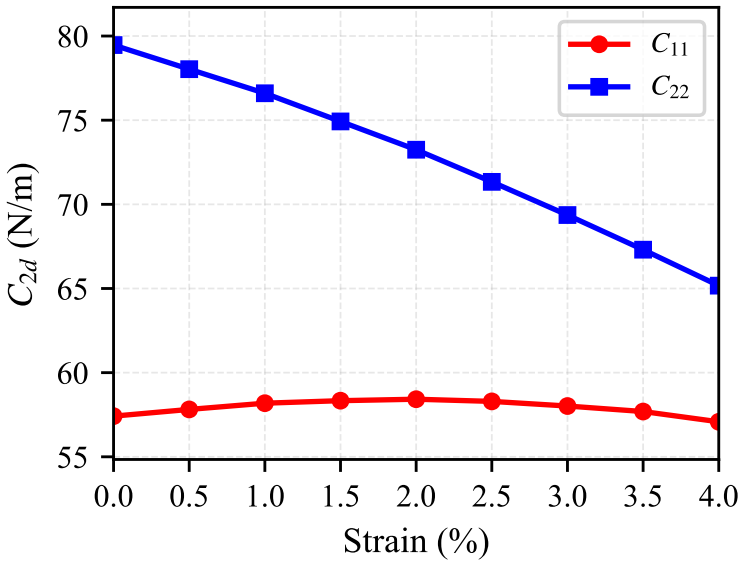

Fig. S9. Elastic constants of PdS_2 monolayer under biaxial strain.

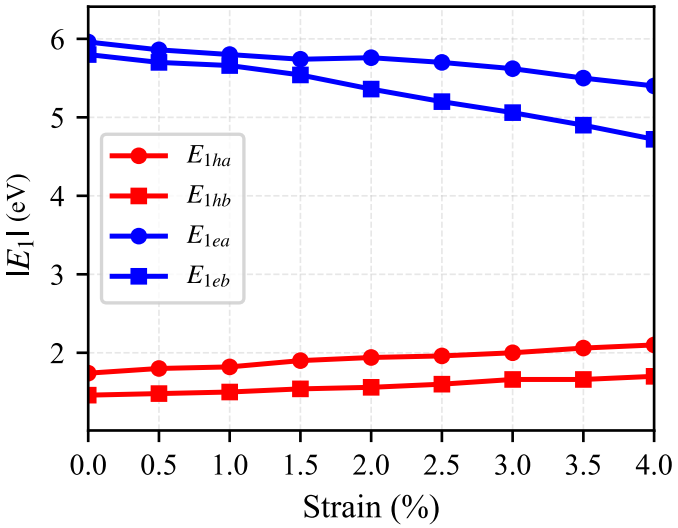

Fig. S10. Deformation potential of PdS_2 monolayer under biaxial strain.

Table S1. Born Effective Charges (unit: e)

Atom	Z_{xx}	Z_{xy}	Z_{xz}	Z_{yx}	Z_{yy}	Z_{yz}	Z_{zx}	Z_{zy}	Z_{zz}
Pd	-0.94	-0.49	-0.02	0.46	-0.86	-0.04	-0.05	0.02	-0.01
Pd	-0.94	0.49	0.02	-0.46	-0.86	-0.04	0.05	0.02	0.01
S	0.47	-0.66	0.17	-0.78	0.43	0.02	0.01	-0.01	0.00
S	0.47	0.66	-0.17	0.78	0.43	0.02	-0.01	-0.01	0.00
S	0.47	0.66	-0.17	0.78	0.43	0.02	-0.01	-0.01	0.00
S	0.47	-0.66	0.17	-0.78	0.43	0.02	0.01	-0.01	0.00

References

[1] Z. H. Levine and D. C. Allan, *Phys. Rev. Lett.*, 1989, **63**, 1719–1722.

[2] V. Fiorentini and A. Baldereschi, *Phys. Rev. B*, 1995, **51**, 17196–17198.

[3] N. M. Regis, J. L. F. Da Silva and M. P. Lima, *ACS Appl. Energy Mater.*, 2025, **8**, 8992–9005.

[4] Y. Ding, U. Mumtaz, I. Khan, N. M. Musyoka, J. Larsson and M. Sajjad, *Appl. Surf. Sci.*, 2026, **720**, 165160.

[5] A. H. Romero, D. C. Allan, B. Amadon, et al., J. Chem. Phys., 2020, 152, 124102.